

# The Moon’s Many Faces: A Single Unified Transformer for Multimodal Lunar Reconstruction

Tom Sander , Moritz Tenthoff , Kay Wohlfarth , Christian Wöhler  
 {tom.sander, moritz.tenthoff, kay.wohlfarth, christian.woehler}@tu-dortmund.de  
 Image Analysis Group, TU Dortmund University, Germany

**Abstract**—Multimodal learning is an emerging research topic across multiple disciplines but has rarely been applied to planetary science. In this contribution, we identify that reflectance parameter estimation and image-based 3D reconstruction of lunar images can be formulated as a multimodal learning problem. We propose a single, unified transformer architecture trained to learn shared representations between multiple sources like grayscale images, digital elevation models, surface normals, and albedo maps. The architecture supports flexible translation from any input modality to any target modality. Predicting DEMs and albedo maps from grayscale images simultaneously solves the task of 3D reconstruction of planetary surfaces and disentangles photometric parameters and height information. Our results demonstrate that our foundation model learns physically plausible relations across these four modalities. Adding more input modalities in the future will enable tasks such as photometric normalization and co-registration.

**Index Terms**—multimodal, lunar surface, digital elevation model (DEM), foundation model, 3D reconstruction, deep learning, any-to-any, height and gradient

## I. INTRODUCTION

MULTIMODAL learning is a subfield of machine learning that aims to integrate and model information from heterogeneous data sources with distinct statistical properties and structures (such as images, spectral data, speech, video, and text), enabling improved performance on complex, real-world tasks. One of the most groundbreaking applications includes vision language models such as DALL-E [3] and GPT-4 [4], [5] that can understand and generate content across image and text modalities. Multimodal learning has rapidly expanded beyond computer vision and natural language processing, finding applications across various disciplines, including healthcare [6], autonomous systems [7], and Earth remote sensing [88], [90]. For the Earth, that could be ambitious goals such as comprehensive visual question answering (VQA) tools that combine geospatial data and language (GeoGPT [2]) or more specific tasks such as sensor fusion [1], denoising [8]–[10], gap-filling [11], [12], and cross-modal prediction [13], [14].

Even though planetary science shares many similarities with Earth science and offers rich and diverse datasets from multiple sensors [89], remote sensing on solar system objects has not yet received much attention from the multimodal machine-learning community. Consequently, investigating which planetary remote sensing tasks can be improved by multimodal learning is both timely and necessary.

Multimodal learning is known to infer cross-modal relationships that improve generalization and robustness [83]–

[85]. In this work we take grayscale images, digital elevation models (DEM), surface normals, and albedo maps as modalities. Multimodal learning allows flexible translation from any input modality to any target modality (any-to-any). Depending on the choice of input(s), individual processing tasks can be formulated. Predicting DEMs and albedo maps from grayscale images solves the 3D reconstruction task of planetary surfaces. Combining surface normals and albedo maps recreates the rendering task, and estimating the albedo from the grayscale image and the topography retrieves the most important photometric parameter.

In the future, adding more modalities (e.g., multiple images, sun and spacecraft geometry) to the unified representation is expected to enable more tasks, such as photometric normalization, and co-registration.

## II. RELATED WORKS

This section first explores previous works on reflectance models, which are the basis for typical lunar remote sensing tasks, such as reflectance normalization and photometric parameter retrieval. Second, we explore different surface reconstruction approaches, highlighting recent machine learning advancements for this task. Third, we will discuss the evolution from unimodal representation learning techniques to more recent multi-modal approaches and their application to remote sensing tasks.

### A. Reflectance Models

A reflectance model is required to normalize measured reflectance data and retrieve surface properties. Reflectance models can be divided into empirical functions and physically motivated analytical models [15]. The simplest approximation is the Lambert model. However, the lunar surface is not isotropic, as the reflectance depends strongly on the phase angle. Instead, the Lambert reflectance is often combined with a phase function and the Minnaert function [16] or Lommel-Seeliger law. McEwen et al. [17] propose the empirical Lunar-Lambert model for photoclinometry and reflectance normalization. Analytical functions model the radiative light transfer and are more accurate but also more computationally expensive [15]. The most prominent models are the Shkuratov [18] and Hapke [19] model. Both model the scattering of light in a particulate medium, i.e., the lunar regolith. The Hapke model is more widely used in planetary science and can therefore be assumed to be the standard model for lunar reflectance [34]. Shepard and Helfenstein [20] perform extensive tests of the

Hapke model and discuss the model inversion for parameter retrieval [21].

### B. Surface Reconstruction

Digital Elevation Model (DEM, sometimes also DTM) generation methods can be grouped into three broad categories: photogrammetry, ranging techniques, and intensity-based methods. More recently, machine learning approaches have emerged that use data from the other methods to generate new DEMs.

Photogrammetry or Stereo vision uses image pairs acquired to compute the disparity between tie-points found by block-matching [22]. The disparities and known camera parameters are used to find the 3D coordinates of the tie-points and interpolate a DEM. Stereo vision is well suited for the creation of global DEMs with high vertical accuracy. However, it is limited by the availability of suitable stereo pairs and the matching process. Due to the size of the matching window, the Ground Sampling Distance (GSD) of the resulting Stereo DEM is typically chosen 3-5 times larger than the GSD of the input images [22], [25]. The actual resolution of the DEM is even coarser due to matching and interpolation errors [22], [24]. Typical reconstruction artefacts include holes in shadowed areas and stair-like structures due to pixel locking [23]. The most commonly used frameworks for Stereo DEM generation are the open source Ames Stereo Pipeline (ASP) [22] and the proprietary SOCET SET from BAE Systems [26].

Ranging techniques include laser altimetry (e.g., the Lunar Orbiter Laser Altimeter (LOLA) [29]) and radar interferometry [30]. The instrument sends out a signal and measures the return time of the reflected signal to determine the distance to the surface. Due to the active nature of the method, it is not dependant on the illumination conditions and can also measure in permanently shadowed regions. The sampling points provide very high vertical accuracy, but the resolution of derived DEMs is limited by the comparatively large cross-track distance between tracks [28] and interpolation artefacts. Barker et al. [28] combined LOLA data with stereo DEMs from the SELENE Terrain Camera [31] to create the SLDEM512 (about 60 m/pixel).

Intensity-based methods relate the intensity of a pixel to the surface orientation and the illumination conditions. Notable early contributions include the works of van Diggelen [38], Rindfleisch [35], Wildey [36], and Kirk [37], who utilized profile- or area-based photoclinometry to determine the shape of planetary surfaces.

Photoclinometry estimates the surface slope, which is subsequently integrated to obtain the surface height. In contrast, Shape from Shading (SfS) methods estimate the surface slope and height simultaneously [41], [44]. However, the terms are often used interchangeably in the literature. Because the reconstruction is based on the surface orientation, the resulting surface slope is very accurate. However, no absolute height information can be retrieved from a single image, and cumulative small integration errors can lead to large deviations from the true surface height [44]. To increase the vertical accuracy Shao et al. [42] introduced a depth constraint to tie

the estimated DEM to a lower resolution initialization. The fusion of SfS with Stereo DEMs and laser altimetry data has been continuously improved over the following years [46]–[49].

The work by Grumpe and Wöhler [43]–[45] builds on previous studies by introducing a more generalized variational approach. They present a new framework that simultaneously estimates surface heights and local reflectance properties, such as the albedo map, using the Hapke reflectance model [19]. Instead of a smoothness constraint, that tends to oversmooth the surface, they use an absolute and relative depth constraint. We utilize this extensively validated [33], [34], [44] SfS framework to generate data for our multimodal model. Other SfS frameworks [50]–[53] use similar approaches to compute DEMs, but often employ simpler reflectance models, smoothness constraints or assume a fixed albedo.

Machine learning techniques can directly infer a relationship between a measured image and a corresponding DEM, created by the methods described above. The trained network can then be used to create entirely new DEMs. Chen et al. [55], [56] use a low-resolution DEM and a high-resolution grayscale image as input to learn a transformation that generates new high-resolution DEMs. To achieve this, the authors utilize two convolutional neural networks (CNN), each representing a different modality, and concatenate the features from these streams to a decoder that generates the DEM. The authors extended their model in [57] and exchanged the high-resolution image branch with a Swin Transformer network [58]. In contrast, our approach unifies multiple paths from different sources into a single model. This means our transformer is not restricted to generating high-resolution DEMs solely from a given grayscale image and an initial low-resolution DEM. In fact, we do not require an initial surface to generate our DEMs. Our broader goal is to learn the correlations between different representations within a single model.

Chen et al. [59] developed Mars3DNet, a CNN-based model designed to generate DEMs of the Martian surface. The model processes the Context Camera (CTX) images as input and employs an auto-denoising network to create a Lambertian image. It then predicts a DEM from this Lambertian image and scales the prediction using an initial low-resolution DEM. In contrast, our approach utilizes a Transformer framework and an any-to-any methodology, allowing our network to produce a broader range of outputs beyond just DEMs.

Tao et al. utilize Generative Adversarial Network (GAN) models in order to create MADNet 1.0 [60] and MADNet 2.0 [61] to generate high-resolution DEMs of the Moon [62] and Mars [63]. In their approach, the authors employ a convolutional U-Net as the generator and a CNN as the discriminator to estimate relative heights from the provided input image. The absolute heights are then obtained by rescaling the predicted relative heights using a low-resolution initial DEM.

A further GAN approach proposed by Cao et al. [64] and Yang et al. [65] combines the U-Net GAN with an attention mechanism utilizing the channel and spatial attention in the U-Net network.

Our approach generally differs from previous models by employing a Transformer architecture, which allows for greater

flexibility and enhanced correlation learning across multiple modalities. Unlike the CNN-based models, which are typically limited to generating specific outputs such as DEMs from single grayscale images, our model supports any-to-any generation, synthesizing varying outputs, including Normal, Albedo, DEM, and more. This holistic perspective broadens the scope of our work, allowing us to investigate and learn inter-modal relationships more effectively.

### C. Multimodal Representation Learning for Remote Sensing

This paper aims to develop a unified representation from various lunar low-level processing tasks by building upon and extending existing representation learning methodologies. Representation learning techniques, such as autoencoders [67], CNNs [66], and VAEs [68], extract meaningful features from raw data by reconstructing inputs or learning data distributions, with newer methods like masked autoencoders [80] excelling at inferring missing information. These approaches have been effectively applied to remote sensing and lunar science, enabling tasks like hyperspectral image classification [69], thermal pattern modeling [70], surface anomaly detection [71], and crater analysis through transfer learning [72], [73].

The field of multimodal learning involves the extension of representation learning to manage multiple data types simultaneously. A common strategy is to convert different modalities into a shared representation format. This often involves the use of modality-specific tokenizers or projection layers, followed by processing through a unified model architecture. Approaches like Multi-MAE [83] utilize shared transformers on projected embeddings from different modalities, while others like 4M [84], [85] employ VQ-VAE [75] tokenizers before utilizing a masked encoder-decoder setup (similar concepts underpin models like Unified-IO [81], [82] for broader data types).

Multi-modal learning is increasingly explored in Earth observation, with works like MMEarth [88], TerraMesh [89], and TerraMind [90] integrating diverse geospatial earth related datasets for enhanced understanding. However, applying such sophisticated multimodal fusion techniques specifically to lunar remote sensing data is an emerging area. Our previous work [86], [87] represents some of the initial efforts in leveraging machine learning to uncover relationships between disparate lunar datasets, with a particular focus on mapping lunar hydration. This paper represents an important initial step in investigate multimodal analysis within lunar studies by developing a more comprehensive multimodal framework for unified low-level task representation.

## III. DATASET

Our dataset consists of six large narrow-angle camera (NAC) images from the Lunar Reconnaissance Orbiter (LRO) [91], [92]. Specifically, these NAC images correspond to the Apollo 11 through 17 landing sites. For the creation of our training dataset, we included images from Apollo 12, 14, 15, 16, and 17 as training samples for our tokenizers and model. By combining and slicing these large images into patches measuring  $224 \times 224$  pixels, with a stride of 32, we generated

Site name:	Image ID:	Incidence angle [°]:	Phase angle [°]:	Nominal Resolution [m]:
Apollo 16	M144524996	47.18	50.98	0.5
Apollo 17	M168000580	45.13	71.15	0.5
Apollo 11	M175124932	40.98	39.86	0.5
Apollo 15	M175252641	49.39	48.43	0.5
Apollo 14	M175388134	44.91	29.33	0.5
Apollo 12	M175428601	45.16	44.03	0.5

TABLE I: All NAC images used in this work are constructed by stitching together both left and right side NAC images and normalizing them using ISIS3 [93].

a total of 1,720,540 images. Since the tokenizers operate with a patch size of 8, this results in 784 tokens per image. As a result, the multimodal model was trained on over 1.34 billion tokens. For testing, we used the NAC image from the Apollo 11 landing site, which yielded 22,405 images to evaluate the algorithm, resulting in over 17 million tokens per modality to test with.

We used our Shape and Albedo from Shading (SfS) framework to derive DEMS, albedo maps, and normal maps from the NAC images. The following paragraph will briefly explain the method which we previously validated for the Moon [44], [45], Mercury [33], and Mars [34]. A more detailed description of the method can be found in [44], [45].

SfS requires a reflectance model  $R$  that relates the shading observed in the image  $I$  to the surface shape, i.e. the DEM representing the surface. A DEM is a function  $z(x, y)$  that assigns a height to each pixel  $(x, y)$ . The components of the surface gradient are the partial derivatives of  $z$  with respect to  $x$  and  $y$ , respectively:

$$p = \frac{\partial z}{\partial x} \quad \text{and} \quad q = \frac{\partial z}{\partial y} \quad (1)$$

The surface normal vector  $\mathbf{n}$  is defined as

$$\mathbf{n} = \frac{1}{\sqrt{p^2 + q^2 + 1}} \begin{pmatrix} -p \\ -q \\ 1 \end{pmatrix} \quad (2)$$

The surface slope angle  $\alpha$  is useful for hazard assessment maps and can be derived from the surface gradient or normal vector with

$$\alpha = \arctan(\sqrt{p^2 + q^2}) = \arccos(n_z) \quad (3)$$

The illumination and viewing geometry is defined by the incidence angle  $i$  (between  $\mathbf{n}$  and  $\mathbf{s}$  pointing to the Sun), the emission angle  $e$  (between  $\mathbf{n}$  and  $\mathbf{v}$  pointing to the camera), and the phase angle  $g$  (between  $\mathbf{s}$  and  $\mathbf{v}$ ). Instead of a simple empirical model (e.g., Lambert or Lunar-Lambert), we opt to use the more complex Hapke model [19]. The Hapke model is a physically based reflectance model that works well for particulate surfaces, such as the lunar regolith. We use the Anisotropic Multiple Scattering Approximation (AMSA) [19] of the Hapke model given by

$$R_{\text{AMSA}}(i, e, g, w) = \frac{w}{4\pi} \frac{\mu_0}{\mu_0 + \mu} [p(g)B_{\text{SH}}(g) + M(\mu_0, \mu)] B_{\text{CB}}(g)S(i, e, g, \bar{\theta}) \quad (4)$$

with  $\mu_0 = \cos(i)$  and  $\mu = \cos(e)$ . The single-scattering albedo  $w$  is the intrinsic reflectivity of the surface material

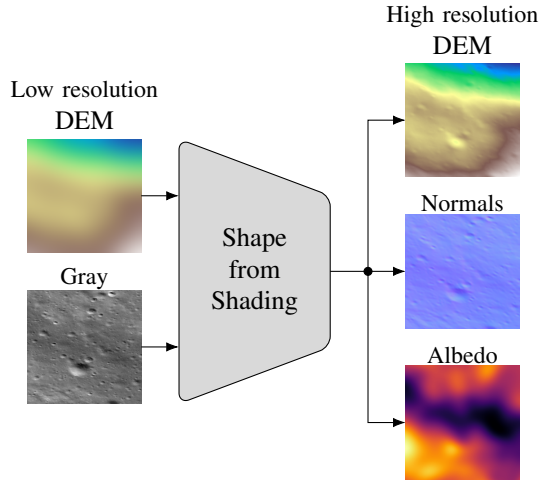


Fig. 1: The SfS algorithm requires a low-resolution DEM and a grayscale image as inputs. The output high-resolution DEM, surface normals, and an albedo map are used as input for the foundation model.

independent of the orientation. Our SfS framework allows us to estimate the pixelwise albedo  $w$  simultaneously with the DEM. The resulting albedo map is used for the multimodal model. We use fixed values estimated by Warell [32] for the remaining parameters of the model. The phase function  $p(g)$  is given by the Double Henyey-Greenstein function with parameters  $b = 0.21$  and  $c = 0.7$  [32]. We use  $B_{S0} = 3.1$  and  $h_S = 0.11$  for the Shadow Hiding Opposition Effect  $B_{SH}$ .

Every SfS algorithm is based on the minimization of the intensity error

$$E_I = \frac{1}{2} \int_x \int_y (R(p, q) - I)^2 dx dy \quad (5)$$

between the modeled reflectance image  $R$  and the observed image  $I$ .

SfS is an ill-posed problem, because two unknowns  $p$  and  $q$  have to be estimated from a single pixel. Therefore, additional regularization terms are required to obtain a solution. The error terms for the SfS algorithm that was used in this work are described in Appendix D. The minimization of the resulting total error is performed using an iterative relaxation approach. The update equations can be found in [44]. Figure 1 shows the input and output of the SfS algorithm. We use the output albedo map, the DEM, and the derived surface normals training and test data for our foundation model.

#### IV. UNIFIED TRANSFORMER APPROACH

In this section, we present a systematic and detailed description of the machine learning methods used. The section is structured into three parts. We start with an overview that explains the overall goal. Next, we delve into the tokenizer section, which outlines how the tokenizers were built and trained. Finally, we discuss the masked autoencoding section, which describes the training procedure of the masked autoencoder.

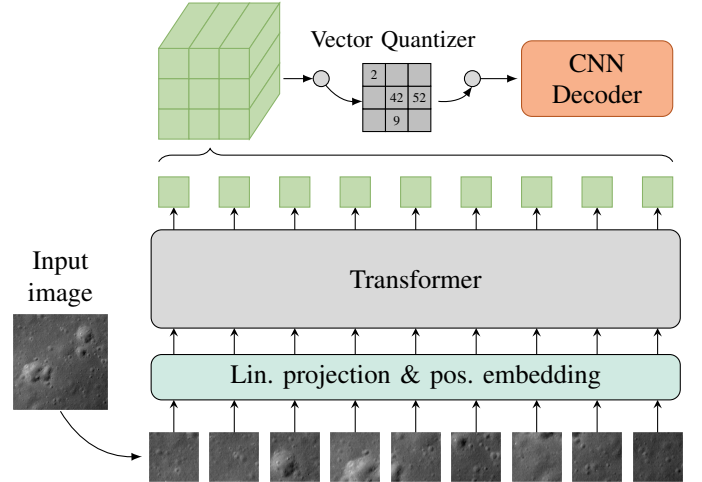


Fig. 2: Custom VQ-Tokenizer [75]: The input image is decoded using a vision transformer [76]. The encoded embeddings are then reshaped to form a cube. After vector quantization, the input cube is decoded using a convolutional neural network.

##### A. General idea

To effectively manage various modalities, such as different sensor inputs, data types, and data sizes within a single model, it is essential to unify these modalities into a consistent dimension. This can be achieved by tokenizing each modality using a modified VQ-Tokenizer [75]. After tokenization, the model is trained in a masked manner to predict the remaining tokens based on a set of unmasked tokens. By training these tokens in a cross-modal fashion, the model learns the different relationships between all modalities. This approach enables the model to understand how to transform, for example, a grayscale image into a digital elevation model.

##### B. Tokenization

We use a custom-built tokenizer structure for the tokenization process, as shown in Figure 2. Specifically, a vision transformer [76] serves as the encoder, while a convolutional neural network (CNN) acts as the decoder to reconstruct the image. The vision transformer, functioning as the encoder, generates a set of embeddings that are reshaped into a three-dimensional cube. This cube is then discretized using a vector quantizer. The quantized vectors within the cube are subsequently processed through the convolutional neural network to reproduce the original input image. We use a Vision Transformer (ViT) [76] as the encoder in combination with the vector quantization (VQ) [75] tokenizer because of its ability to extract rich and contextual features from images. By utilizing the self-attention mechanism, the ViT effectively captures long-range dependencies and non-local relationships among different image parts. This results in more informative and robust feature representations. Consequently, our VQ tokenizer can learn a more effective and compact representation of the input image, which is crucial for achieving high-quality image reconstruction and compression.

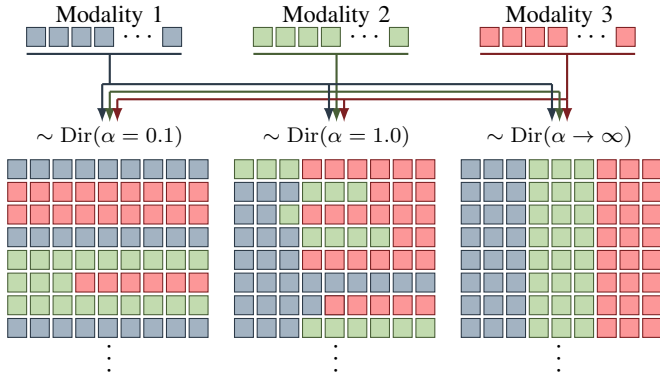


Fig. 3: Figure illustrates the Dirichlet sampling process for a set of three distinct modalities, similar to the approach described in [83]. When the  $\alpha$  parameter is low, only one modality, or occasionally just a few tokens from a single modality, is selected for training, while the remaining tokens serve as targets. When  $\alpha$  is set to 1.0, a diverse mixture of tokens from all modalities is sampled each time. Conversely, as  $\alpha$  approaches  $\infty$ , the sampling results in a uniform distribution across all modalities.

### C. Masked Autoencoding

Developing an effective masking strategy to train and obtain a robust and meaningful representation of input data is essential. For this purpose, we employ the same masking strategy as detailed in [83]–[85]. This strategy, illustrated in Figure 3, involves a Dirichlet sampling process with a hyperparameter  $\alpha$ . When  $\alpha$  is set to a small value, the process primarily samples from a single modality and aims to predict the remaining modalities. If  $\alpha$  is close to 1, the sampled input token sequences will be more diverse. Conversely, as  $\alpha$  increases, the resulting input token sequences converge towards a uniform sampling of all available modalities.

Another important aspect of the multi-modal masked autoencoder is pre-training. This step involves training one modality using another, which helps in learning a representation of these two initial modalities. The pre-training is conducted on a smaller model, while the other modalities are fine-tuned into a slightly larger model with an increased sequence length after the pre-training is completed.

Figure 4 illustrates the overall architecture of the model. This figure shows that the tokenizers first decompose the input maps (modalities) into tokens. These tokens are then fed into the encoder and diffusion decoder [77] networks. The encoder network uses an input mask, while the diffusion decoder uses a target mask. The output embeddings produced by the encoder serve as context for the decoder in the cross-attention layers [74], where the attention is defined as [74]:

$$\text{Attention}(Q, K, V) = \text{softmax} \left( \frac{Q \cdot K^T}{\sqrt{d_k}} \right) \cdot V \quad (6)$$

while the query matrix  $Q$  is constructed using the decoder vectors, along with the key matrix  $K$  and the value matrix  $V$  from the encoder’s output embeddings. This approach enables

the diffusion decoder to predict the remaining target tokens by leveraging the context provided by the encoder.

The system is trained with a modality-wise loss function, which is defined as:

$$\mathcal{L}_{\text{modality}} = \sum_{i=1}^{N_{\text{mods}}} \text{CE}(\hat{y}_{\text{mod}} || y_{\text{mod}}) \quad (7)$$

where  $\hat{y}_{\text{mod}}$  is the predicted output of the model,  $y_{\text{mod}}$  is the target output, and  $N_{\text{mods}}$  is the number of modalities. The loss function is computed using the cross-entropy (CE) between the predicted and target tokens for each modality. This approach allows the model to learn from the relationships between different modalities and improve its performance in multi-modal tasks.

## V. TRAINING AND EVALUATION

### A. Training Pipeline

One challenge in training a multimodal system is incorporating many modalities into one model. A promising approach is to pre-train the system using two modalities, such as grayscale images and DEMs, and then fine-tune it with additional modalities.

This pre-training on two modalities enables the system to learn their fundamental relationships. Once these relationships are established, the system can be fine-tuned with more modalities to enhance its performance.

We first pre-trained a smaller model using a sequence length of 1568 to train our model. This model randomly utilized either the grayscale tokens or the DEM (Digital Elevation Model) tokens as input, aiming to reproduce the corresponding modality. By doing so, we constructed an autoencoder that learns to integrate Shape from Shading and image rendering, allowing us to generate the DEM from the grayscale image or vice versa.

Once we have established this foundation, we incorporate the normal vectors into the model by adjusting the  $\alpha$  values explained in Section IV. These values dictate the distribution of input modality tokens and are set to more meaningful levels based on the specific modality. Generally, we assign a low  $\alpha$  value to the modalities *Gray* and *DEM* while the  $\alpha$  value for the modality *Normals* is set higher. This approach allows the training to primarily include the *Gray* and *DEM* tokens while intermittently incorporating the *Normals* tokens into the model. As a result, the transformer continuously integrates knowledge about the normal vectors while maintaining the understanding of the grayscale to DEM transformation.

Lastly, we incorporate the *Albedo* feature into the transformer using the same strategy as outlined above. To enable the generation of one modality out of three given modalities, we increase the sequence length from 1568 to 2352 (calculated as 784 tokens per image multiplied by 3). We then copy the available weights from the smaller transformer to the larger one. After this, we maintain the previous configuration while adding a higher  $\alpha$  value for the *Albedo* modality. This approach allows the Albedo modality to be incorporated into the transformer gradually, ensuring that the previous knowledge is preserved.

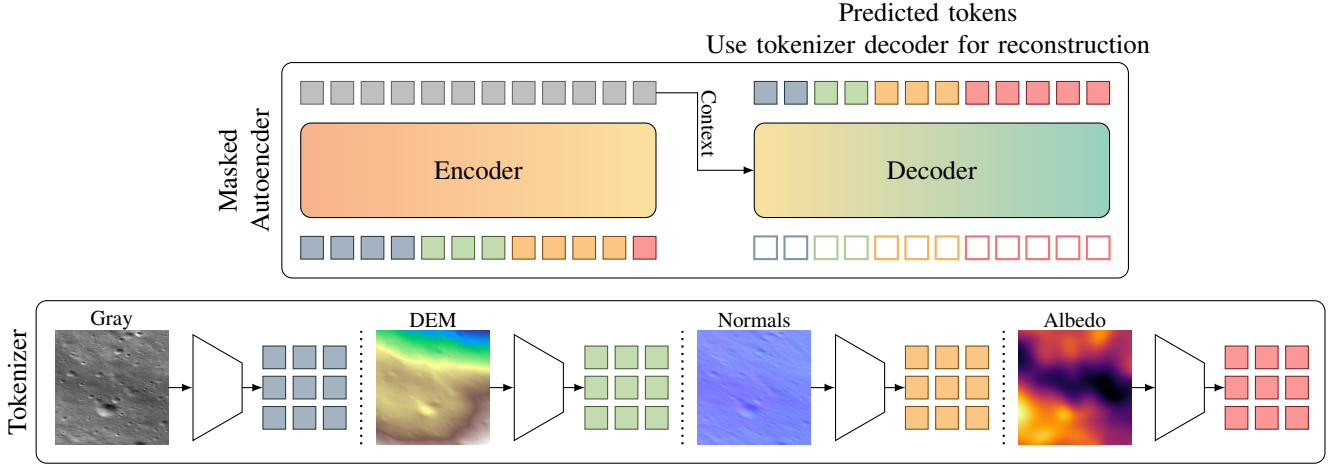


Fig. 4: The figure illustrates the training process of the Multimodal Masked Autoencoder. Initially, different input modalities are tokenized, and some tokens are masked. The unmasked tokens are fed into the encoder, while the decoder predicts the masked tokens. During evaluation, these predicted tokens are decoded back to their original form using the decoder from the specific tokenizer for each modality.

## B. Evaluation Metrics

In this section, we will outline the metrics used to evaluate our multimodal any-to-any approach. The evaluation is divided into two parts: qualitative and quantitative.

1) *Qualitative metrics*: We will first assess our results qualitatively by showcasing various predictions, demonstrating cross-modal retrieval, and conducting ablation studies on specific data points. Additionally, we will visualize the attention mechanism to provide further insights.

2) *Quantitative metrics*: The quantitative metrics are classified into three categories: pixel-wise, modal-wise, and token-wise. For pixel-wise metrics, we will employ the following measures between the input image  $x(i, j)$  and the predicted image  $\hat{x}(i, j)$ :

- **Mean Squared Error (MSE)**:

$$\text{MSE}(x, \hat{x}) = \frac{1}{mn} \sum_{i=1}^n \sum_{j=1}^m [x(i, j) - \hat{x}(i, j)]^2 \quad (8)$$

- **Root Mean Squared Error (RMSE)**:

$$\text{RMSE}(x, \hat{x}) = \sqrt{\text{MSE}(x, \hat{x})} \quad (9)$$

- **Peak Signal-to-Noise Ratio (PSNR)**:

$$\text{PSNR}(x, \hat{x}) = 20 \log_{10} \left( \frac{\text{MAX}_x}{\sqrt{\text{MSE}(x, \hat{x})}} \right) \quad (10)$$

- **Structural Similarity Index (SSIM)**:

$$\text{SSIM}(x, y) = \frac{(2\mu_x\mu_y + c_1)(2\sigma_{xy} + c_2)}{(\mu_x^2 + \mu_y^2 + c_1)(\sigma_x^2 + \sigma_y^2 + c_2)} \quad (11)$$

We will conduct both an ablation study and a cross-modal retrieval study to evaluate the quality of the joint embedding space and determine each modality's contributions to the model's performance. We will analyze the relevant metrics in various scenarios, including cases where one or multiple modalities are absent and only a single remaining modality is used for prediction.

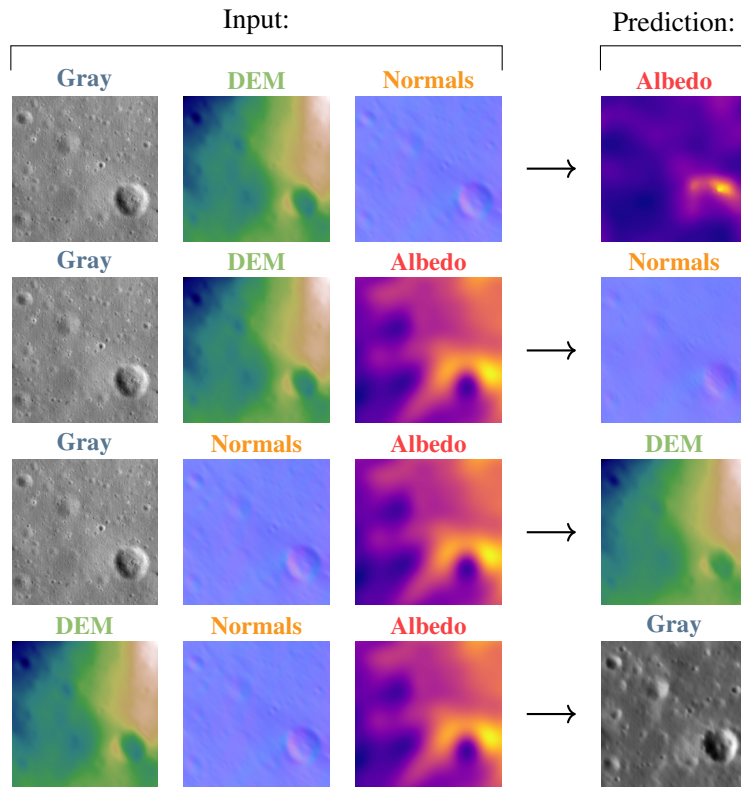
## VI. RESULTS

### A. Qualitative results

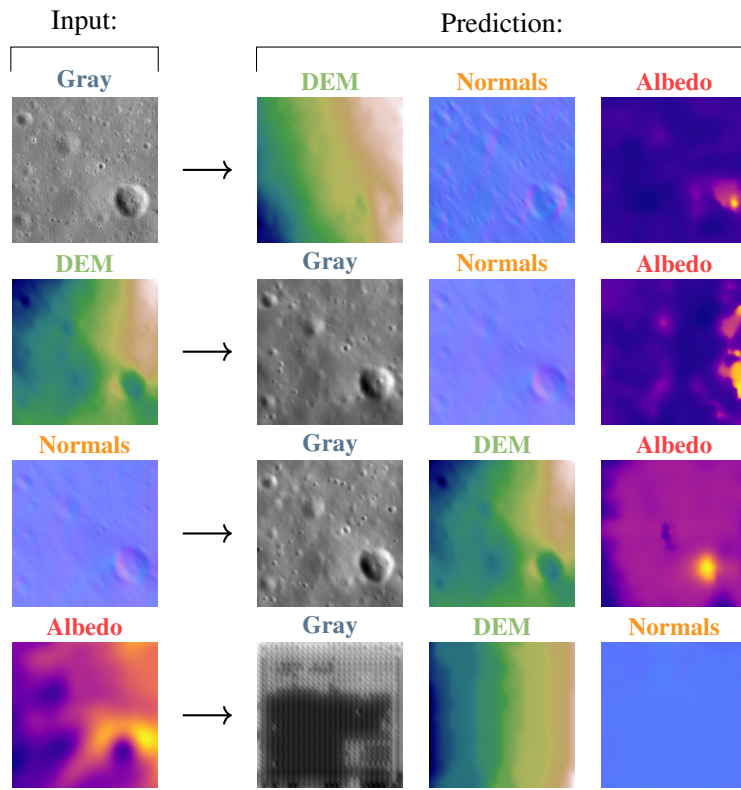
Figure 5 presents two scenario predictions from the Apollo 11 landing site test dataset. In Figure 5a, all three modalities are provided, and the remaining missing modalities are being predicted. The qualitative analysis indicates a significant reconstruction of the missing modality. Conversely, Figure 5b illustrates a scenario where predictions for all three missing modalities are made using just one modality. This approach works well qualitatively for the first three modalities (grayscale images, normal maps, and Digital Elevation Models), but it fails in the last case, where the predictions are derived from the albedo modality. This outcome is expected, as there is no direct relationship between the albedo map and the other modalities, highlighting the model's ability to learn only valid correlations.

One effective way to explore the relationships between different modalities is by visualizing the attention mechanism. The Attention Map, which is created by computing the dot product of features, is generated from the network across all layers and then averaged over each pixel. Consequently, a single forward pass yields one Attention Map. To capture all relationships, we store the Attention Maps for all available test images and then average them across all pixels. Since the Transformer has an input sequence length of 2,352 tokens (which equals  $784 \times 3$ ), we input all possible combinations of three inputs to predict the remaining one. This process results in the Attention Maps shown in Figure 6.

The attention maps displayed show bright colors along the diagonal, while the remaining matrix exhibits varying brightness levels. It is also evident that the tokens within the same modality (the diagonal boxes) are more highly correlated than tokens representing intermodality relationships.



(a) Predicting one remaining modality from three input modalities



(b) Predicting three modalities from a single input modality

Fig. 5: Predictions of the multimodal model. The model generates in the first case one remaining modality while predicting in the second case all remaining modalities from a single one.

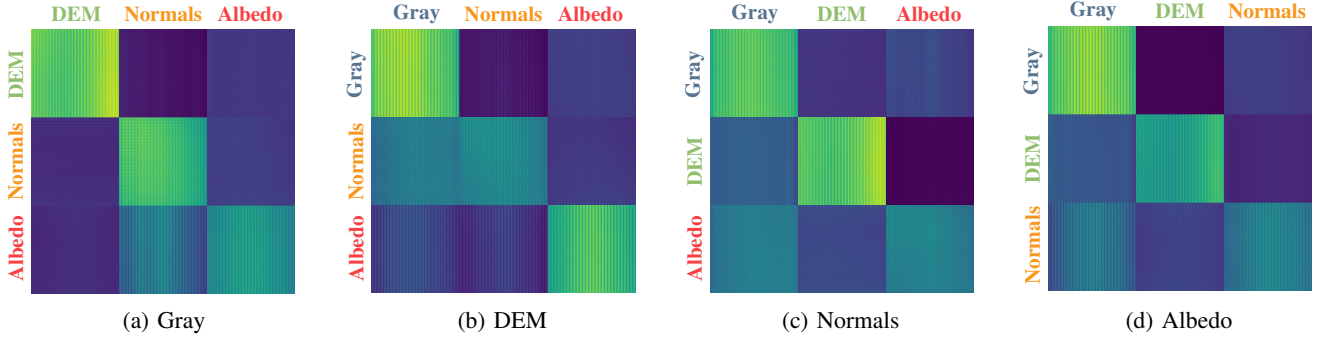


Fig. 6: The subfigures above present the summed attention maps for the available data points in the test dataset. The transformer model is evaluated using three different input modalities, aiming to predict the remaining modality. All attention maps generated from this process are stacked on top of one another and then summed, resulting in the four images displayed above.

### B. Quantitative results

In the following sections, we will first discuss the quantitative results for the scenario where three modalities are used to predict one remaining modality. Next, we will examine the results for the case in which a single modality is used to predict the remaining three modalities.

Modality:	MSE	RMSE	PSNR	SSIM	Datarange
Gray [I/F]	0.091	0.3013	37.2737	0.726185	0.09827
DEM [m]	3780.708	61.4874	52.1714	0.955542	355.6104
Normals	34.849	5.9033	41.4265	0.917043	2.0
Albedo	60.004	7.7462	14.2597	0.932345	0.0801

TABLE II: Quantitative pixelwise metrics for the multimodal model. For the case that three modalities are used to predict one remaining modality. The table shows the Mean Squared Error (MSE), Root Mean Squared Error (RMSE), Peak Signal-to-Noise Ratio (PSNR), and Structural Similarity Index (SSIM) for each predicted modality.

1) *Predicting the Remaining Modality*: The results for the first scenario (predicting one modality from three) are presented in Table II. In this table, the modalities listed represent the single remaining (predicted) modality. We use several metrics to evaluate performance: MSE/RMSE to measure absolute error, PSNR to assess the noise ratio, and SSIM to evaluate perceptual similarity. The model shows varying levels of success, indicating that the relationships between the input modalities and the target modality differ in complexity and predictability.

Specifically, for the grayscale image, it exhibits a low mean squared error (MSE) and root mean squared error (RMSE). However, it also has a limited value range. Additionally, the grayscale modality has the lowest structural similarity index (SSIM) value, suggesting that while the pixel-wise error may be minimal, there are slight discrepancies in the structural (perceived) details.

The DEM, on the other hand, has a much higher MSE/RMSE value, which is not surprising given that the DEM values range between several hundred meters. To measure the SSIM metric between two images, it is necessary for the values to be in the range of 0 to 1. Therefore, to compute the SSIM between the predicted and the ground truth DEM, we apply

a Lambertian Reflectance model [94] to shade both images and transform them into the 0 to 1 range. Here, we observe the highest SSIM value, indicating that the model successfully captured the structural patterns and relative heights.

Upon examining the results of the Normal Vectors, we find that the MSE and RMSE are in the moderate range. Additionally, the PSNR is midrange when compared to other modalities. However, it is noteworthy that the model achieves a high SSIM, indicating that it effectively captures the orientation and direction of the surface. One of the contributing inputs to this analysis is the DEM, which provides this information.

Lastly, we examine the results of the Albedo map. Here, we found that the MSE and Root RMSE values were surprisingly high, especially considering the narrow value range of zero to one. This indicates a significant discrepancy in pixel intensity, leading to a notably low PSNR. However, it is important to note that the SSIM remained high, indicating that the algorithm effectively captured the spatial distribution and patterns of reflectivity on the lunar surface. These findings are also clearly illustrated in Figure 5.

In conclusion, the model consistently yields high SSIM values across all modalities, indicating that the algorithm effectively preserves structural information and captures the underlying relationships.

2) *Predicting All Remaining Modalities from a Single Modality*: In this subsection, we evaluate the model’s effectiveness in predicting remaining modalities using a single input modality, as illustrated in Figure 7. Darker green in each subfigure indicates better performance across all three metrics.

Starting with the SSIM metric in Figure 7a, the strongest predictions are seen when estimating the Digital Elevation Model (DEM) from normals and vice versa. In contrast, the weakest predictions occur when trying to derive normals from the albedo map.

For the PSNR metric, the relationship between normals and DEM remains strong, while predictions involving albedo generally yield lower PSNR values, particularly when albedo is the target.

The RMSE analysis shows that the gray modality leads to the lowest errors despite having a small range in values. Comparatively, the grayscale image outperforms the albedo

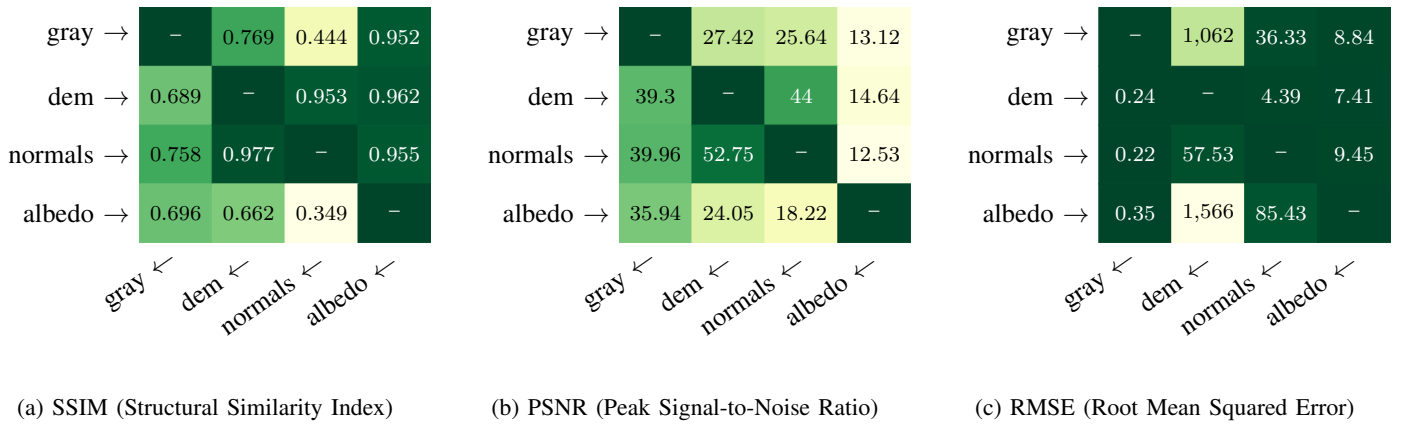


Fig. 7: Heatmap visualization of cross-modal relationships, when predicting *all modalities from a single one*. All Heatmap show on the x-axis the predicted modality and on the y-axis the input modality. The first column shows the SSIM metric, the second column shows the PSNR metric, and the last column shows the RMSE metric.

modality. The DEM has the highest error but also the broadest value range.

These metrics reveal a significant geometric correlation between the DEM and normals, as the latter derives from the DEM’s gradient. Predictions from DEM to normals yield high SSIM, high PSNR, and low RMSE, whereas the reverse shows high SSIM and high PSNR but struggles with absolute heights, resulting in a higher RMSE.

The albedo’s weak correlation with geometry is evident, as predictions involving albedo show low SSIM and high RMSE values, indicating that reflectivity alone is insufficient for accurate geometric determination.

The gray image acts as a complex composite signal incorporating geometry, reflectivity, and lighting, leading to successful predictions. However, predicting the DEM from grayscale presents challenges due to the ambiguity typical of Shape from Shading.

Interestingly, predicting the albedo from the grayscale image demonstrates high SSIM but low PSNR, highlighting the difficulty in isolating intrinsic reflectivity from shading effects. While a surprisingly high SSIM of 0.962 is observed between DEMs and albedo, the low PSNR of 14.64 suggests the model leans on statistical correlations.

Overall, DEMs and surface normals provide valuable information for predicting each other, especially regarding structural characteristics, but albedo is an insufficient predictor of geometric properties, complicating the prediction of specific components from the composite gray signal due to inherent ambiguities.

Directly comparing the accuracy of our DEM with that of other studies using the RMSE presents inherent challenges. As we have noted, RMSE is an absolute measure that is closely tied to the specific characteristics of our study site. Furthermore, utilizing these metrics at the highest available resolution often lacks a directly comparable ground truth dataset. Previous research [33], [34] has tackled this issue by employing scale invariance, where Shape from Shading (SfS) is applied to lower-resolution imagery and validated against higher-resolution stereo data. As a result, a direct comparison

using stereo data of the same high resolution or laser altimetry points may not provide the most meaningful evaluation of relative performance across different methodologies.

To provide a more standardized and comparable evaluation, we examined the SSIM. Our method achieved a high SSIM of up to 76.9% (Grayscale to DEM prediction). This result indicates a strong structural similarity when compared to other DEM generation approaches, which is higher than those of Yang et al. with 60.8% [65] but lower than MadNet2 [61], which achieved an SSIM value of 93%.

3) *Predicting remaining modalities’ error terms*: Upon reviewing Figure 8, we can observe trends that are similar to those discussed in the previous section. The four subfigures display absolute error terms as violin plots, which illustrate the distribution of errors along the vertical axis. Each subfigure represents the prediction error for a specific modality while using different input modalities. This approach allows us to compare the prediction error of a given modality when predicted from all other modalities.

The first noticeable trend is the synergy between the DEM and surface normals, which was highlighted in the previous section. Figures 8b and 8c demonstrate that this combination yields the lowest median error and the most compact distribution compared to the other inputs.

In contrast, the albedo map proves to be a poor predictor of geometry. This conclusion is evident in Figures 8b and 8c, where the albedo input shows the highest median error and the broadest distribution.

Furthermore, the results related to the grayscale images are apparent in the plots of Figure 8a. Here, it is clear that predicting the grayscale image from either the DEM or the normals is quite successful, whereas predicting it from the albedo map is much more challenging, resulting in a higher error and broader distribution.

Lastly, predicting the albedo itself seems generally difficult (see figure 8d), with relatively high median errors and wide distributions, regardless of the input used. The only exception is that predicting the albedo map from the grayscale image appears to be slightly more successful than predictions made

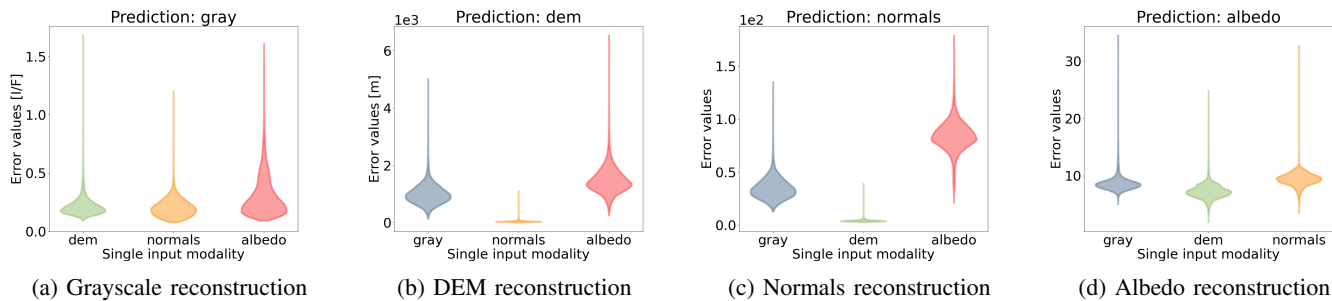


Fig. 8: This illustration displays the error visualization of cross-modal relationships when predicting *all modalities from a single input modality*. Each subfigure represents the error distribution of the predicted modality, based on predictions made from one input modality (shown on the x-axis). The error distributions are organized according to the predicted modality, so the labels on the x-axis indicate from which modality the prediction was made.

from the normals or DEM. Again, this is reasonable since the albedo is largely independent of the surface shape.

## VII. CONCLUSION

This work demonstrates the potential of multimodal learning to unify computer vision tasks in lunar remote sensing. Our model successfully reconstructs missing modalities by exploiting cross-modal relationships between grayscale images, DEMs, surface normals, and albedo maps, effectively performing tasks like 3D reconstruction and photometric parameter estimation. Our qualitative results demonstrate strong reconstruction capabilities, which is particularly evident when predicting from three modalities to one remaining modality. Further, our quantitative metrics (SSIM, PSNR, and RMSE) demonstrate a strong geometric correlation between DEMs and normals, with predictions between these two modalities achieving high accuracy. This strong dependence was consistent across all metrics. In contrast, albedo exhibits a limited correlation with geometric modalities, highlighting the physical independence of surface reflectivity from topography. Furthermore, it became clear that grayscale images serve as a complex composite signal combining effects of geometry, reflectivity, and lighting. While high SSIM values generally confirm the preservation of crucial structural details, challenges persist in accurately predicting absolute DEM heights. These findings validate the multimodal learning approach for lunar data analysis, especially when facing incomplete datasets. Future work will expand this unified framework by incorporating more modalities to tackle additional tasks like photometric normalization and co-registration.

## REFERENCES

- [1] J. Li et al., "Deep learning in multimodal remote sensing data fusion: A comprehensive review," *International Journal of Applied Earth Observation and Geoinformation*, vol. 112. Elsevier BV, p. 102926, Aug. 2022. doi: 10.1016/j.jag.2022.102926.
- [2] Y. Zhang, C. Wei, Z. He, and W. Yu, "GeoGPT: An assistant for understanding and processing geospatial tasks," *International Journal of Applied Earth Observation and Geoinformation*, vol. 131. Elsevier BV, p. 103976, Jul. 2024. doi: 10.1016/j.jag.2024.103976.
- [3] K. Lin, Z. Yang, L. Li, J. Wang, and L. Wang, "DEsignBench: Exploring and Benchmarking DALL-E 3 for Imagining Visual Design," 2023, arXiv. doi: 10.48550/ARXIV.2310.15144.
- [4] A. Radford, J. Wu, R. Child, D. Luan, D. Amodei, and I. Sutskever, "Language Models are Unsupervised Multitask Learners," OpenAI, 2019. [Online]. Available: [https://cdn.openai.com/better-language-models/language\\_models\\_are\\_unsupervised\\_multitask\\_learners.pdf](https://cdn.openai.com/better-language-models/language_models_are_unsupervised_multitask_learners.pdf)
- [5] OpenAI et al., "GPT-4 Technical Report," 2023, arXiv. doi: 10.48550/ARXIV.2303.08774.
- [6] F. Krones, U. Marikkar, G. Parsons, A. Szmul, and A. Mahdi, "Review of multimodal machine learning approaches in healthcare," *Information Fusion*, vol. 114. Elsevier BV, p. 102690, Feb. 2025. doi: 10.1016/j.inffus.2024.102690.
- [7] J. Li, J. Li, G. Yang, L. Yang, H. Chi, and L. Yang, "Applications of Large Language Models and Multimodal Large Models in Autonomous Driving: A Comprehensive Review," *Drones*, vol. 9, no. 4. MDPI AG, p. 238, Mar. 24, 2025. doi: 10.3390/drones9040238.
- [8] A. Maffei, J. M. Haut, M. E. Paoletti, J. Plaza, L. Bruzzone, and A. Plaza, "A Single Model CNN for Hyperspectral Image Denoising," *IEEE Transactions on Geoscience and Remote Sensing*, vol. 58, no. 4. Institute of Electrical and Electronics Engineers (IEEE), pp. 2516-2529, Apr. 2020. doi: 10.1109/tgrs.2019.2952062.
- [9] Q. Yuan, Q. Zhang, J. Li, H. Shen, and L. Zhang, "Hyperspectral Image Denoising Employing a Spatial-Spectral Deep Residual Convolutional Neural Network," *IEEE Transactions on Geoscience and Remote Sensing*, vol. 57, no. 2. Institute of Electrical and Electronics Engineers (IEEE), pp. 1205-1218, Feb. 2019. doi: 10.1109/tgrs.2018.2865197.
- [10] L. Han, Y. Zhao, H. Lv, Y. Zhang, H. Liu, and G. Bi, "Remote Sensing Image Denoising Based on Deep and Shallow Feature Fusion and Attention Mechanism," *Remote Sensing*, vol. 14, no. 5. MDPI AG, p. 1243, Mar. 03, 2022. doi: 10.3390/rs14051243.
- [11] M. Appel, "Efficient Data-Driven Gap Filling of Satellite Image Time Series Using Deep Neural Networks with Partial Convolutions," *Artificial Intelligence for the Earth Systems*, vol. 3, no. 2. American Meteorological Society, Apr. 2024. doi: 10.1175/aies-d-22-0055.1.
- [12] Á. Moreno-Martínez et al., "Multispectral high resolution sensor fusion for smoothing and gap-filling in the cloud," *Remote Sensing of Environment*, vol. 247. Elsevier BV, p. 111901, Sep. 2020. doi: 10.1016/j.rse.2020.111901.
- [13] F. Liu et al., "RemoteCLIP: A Vision Language Foundation Model for Remote Sensing," *IEEE Transactions on Geoscience and Remote Sensing*, vol. 62. Institute of Electrical and Electronics Engineers (IEEE), pp. 1-16, 2024. doi: 10.1109/tgrs.2024.3390838.
- [14] Vivanco Cepeda, V., Nayak, G.K. and Shah, M., 2023., "Geoclip: Clip-inspired alignment between locations and images for effective worldwide geo-localization," *Advances in Neural Information Processing Systems*, vol. 36, pp.8690-8701.
- [15] M. K. Shepard, *Introduction to planetary photometry*. 2017. doi: 10.1017/9781316443545.
- [16] M. Minnaert, "The reciprocity principle in lunar photometry," *The Astrophysical Journal*, vol. 93, p. 403, May 1941, doi: 10.1086/144279.
- [17] A. S. McEwen, "Photometric functions for photoclinometry and other applications," *Icarus*, vol. 92, no. 2, pp. 298-311, Aug. 1991, doi: 10.1016/0019-1035(91)90053-v.
- [18] Y. Shkuratov, L. Starukhina, H. Hoffmann, and G. Arnold, "A model of spectral albedo of particulate surfaces: Implications for optical properties of the Moon," *Icarus*, vol. 137, no. 2, pp. 235-246, Feb. 1999, doi: 10.1006/icar.1998.6035.

- [19] B. Hapke, "Theory of Reflectance and Emittance Spectroscopy," Cambridge University Press, 2012.
- [20] M. K. Shepard and P. Helfenstein, "A test of the Hapke photometric model," *Journal of Geophysical Research Atmospheres*, vol. 112, no. E3, Feb. 2007. doi: 10.1029/2005je002625.
- [21] P. Helfenstein and M. K. Shepard, "Testing the Hapke photometric model: Improved inversion and the porosity correction," *Icarus*, vol. 215, no. 1, pp. 83-100, Jul. 2011. doi: 10.1016/j.icarus.2011.07.002.
- [22] R. A. Beyer, O. Alexandrov, and S. McMichael, "The Ames Stereo Pipeline: NASA's Open Source Software for Deriving and Processing Terrain Data," *Earth and Space Science*, vol. 5, no. 9. American Geophysical Union (AGU), pp. 537-548, Sep. 2018. doi: 10.1029/2018ea000409.
- [23] S. Gehrig and U. Franke, "Stereovision for ADAS," *Handbook of Driver Assistance Systems*. Springer International Publishing, pp. 495-524, Dec. 08, 2015. doi: 10.1007/978-3-319-12352-3\_22.
- [24] R. L. Kirk et al., "COMMUNITY TOOLS FOR CARTOGRAPHIC AND PHOTOGRAMMETRIC PROCESSING OF MARS EXPRESS HRSC IMAGES," *The International Archives of the Photogrammetry, Remote Sensing and Spatial Information Sciences*, vol. XLII-3/W1. Copernicus GmbH, pp. 69-76, Jul. 25, 2017. doi: 10.5194/isprs-archives-xxlii-3-w1-69-2017.
- [25] R. L. Kirk et al., "Evaluating Stereo Digital Terrain Model Quality at Mars Rover Landing Sites with HRSC, CTX, and HiRISE Images," *Remote Sensing*, vol. 13, no. 17. MDPI AG, p. 3511, Sep. 04, 2021. doi: 10.3390/rs13173511.
- [26] Miller, S. B., and A. S. Walker. "Further developments of Leica digital photogrammetric systems by Helava." *Acsm Asprs Annual Convention*. Vol. 3. American Soc Photogrammetry & Remote Sensing+ Amer Cong On, 1993.
- [27] F. Scholten et al., "GLD100: The near-global lunar 100 m raster DTM from LROC WAC stereo image data," *Journal of Geophysical Research: Planets*, vol. 117, no. E12. American Geophysical Union (AGU), Mar. 30, 2012. doi: 10.1029/2011je003926.
- [28] Barker, M. K., et al., "A new lunar digital elevation model from the Lunar Orbiter Laser Altimeter and SELENE Terrain Camera," *Icarus* 273 (2016): 346-355.
- [29] D. E. Smith et al., "The Lunar Orbiter Laser Altimeter Investigation on the Lunar Reconnaissance Orbiter Mission," *Space Science Reviews*, vol. 150, no. 1-4. Springer Science and Business Media LLC, pp. 209-241, May 16, 2009. doi: 10.1007/s11214-009-9512-y.
- [30] S. Hensley et al., "An improved map of the lunar south pole with earth based radar interferometry," 2008 IEEE Radar Conference. IEEE, pp. 1-6, May 2008. doi: 10.1109/radar.2008.4721077.
- [31] J. Haruyama et al., "Planned radiometrically calibrated and geometrically corrected products of lunar high-resolution Terrain Camera on SELENE," *Advances in Space Research*, vol. 42, no. 2. Elsevier BV, pp. 310-316, Jul. 2008. doi: 10.1016/j.asr.2007.04.062.
- [32] J. Warell, "Properties of the Hermean regolith: IV. Photometric parameters of Mercury and the Moon contrasted with Hapke modelling," *Icarus*, vol. 167, no. 2. Elsevier BV, pp. 271-286, Feb. 2004. doi: 10.1016/j.icarus.2003.10.010.
- [33] M. Tenthoff, K. Wohlfarth, and C. Wöhler, "High Resolution Digital Terrain Models of Mercury," *Remote Sensing*, vol. 12, no. 23. MDPI AG, p. 3989, Dec. 06, 2020. doi: 10.3390/rs12233989.
- [34] M. Hess, M. Tenthoff, K. Wohlfarth, and C. Wöhler, "Atmospheric Correction for High-Resolution Shape from Shading on Mars," *Journal of Imaging*, vol. 8, no. 6. MDPI AG, p. 158, Jun. 01, 2022. doi: 10.3390/jimaging8060158.
- [35] Rindfleisch, T., "Photometric method for lunar topography," *Photogrammetric Engineering* 32, no. 2, 1966, p. 262-277.
- [36] R. Wildey, "Generalized photoclinoetry for Mariner 9," *Icarus*, vol. 25, no. 4. Elsevier BV, pp. 613-626, Aug. 1975. doi: 10.1016/0019-1035(75)90043-3.
- [37] R. L. Kirk and D. J. Stevenson, "Thermal evolution of a differentiated Ganymede and implications for surface features," *Icarus*, vol. 69, no. 1. Elsevier BV, pp. 91-134, Jan. 1987. doi: 10.1016/0019-1035(87)90009-1.
- [38] J. van Diggelen, "A photometric investigation of the slopes and the heights of the ranges of hills in the Maria of the Moon," *Bulletin of the Astronomical Institutes of the Netherlands*, vol. 11, p. 283, Jul. 1951.
- [39] B. K. P. Horn, "Shape from shading: A method for obtaining the shape of a smooth opaque object from one view," 1970.
- [40] B. K. P. Horn, "Image intensity understanding," Aug. 1975.
- [41] B. K. P. Horn, "Height and gradient from shading," *International Journal of Computer Vision*, vol. 5, no. 1. Springer Science and Business Media LLC, pp. 37-75, Aug. 1990. doi: 10.1007/bf00056771.
- [42] M. Shao, R. Chellappa, and T. Simchony, "Reconstructing a 3-D depth map from one or more images," *CVGIP: Image Understanding*, vol. 53, no. 2. Elsevier BV, pp. 219-226, Mar. 1991. doi: 10.1016/1049-9660(91)90029-o.
- [43] C. Wöhler and A. Grumpe, "Integrated DEM Construction and Calibration of Hyperspectral Imagery: A Remote Sensing Perspective," *Mathematics and Visualization*. Springer Berlin Heidelberg, pp. 467-492, Nov. 26, 2012. doi: 10.1007/978-3-642-34141-0\_21.
- [44] A. Grumpe, F. Belkhir, and C. Wöhler, "Construction of lunar DEMs based on reflectance modelling," *Advances in Space Research*, vol. 53, no. 12. Elsevier BV, pp. 1735-1767, Jun. 2014. doi: 10.1016/j.asr.2013.09.036.
- [45] A. Grumpe and C. Wöhler, "Recovery of elevation from estimated gradient fields constrained by digital elevation maps of lower lateral resolution," *ISPRS Journal of Photogrammetry and Remote Sensing*, vol. 94. Elsevier BV, pp. 37-54, Aug. 2014. doi: 10.1016/j.isprsjprs.2014.04.011.
- [46] L. A. Soderblom and R. L. Kirk, "Meter-Scale 3-D Models of the Martian Surface from Combining MOC and MOLA Data," *Lunar and Planetary Science Conference*, p. 1730, Jan. 2003.
- [47] R. Danzl, H. Fassold, K. Schindler, and H. Bischof, "Reconstruction of Archaeological Finds using Shape from Stereo and Shape from Shading," pp. 21-30, Jan. 2004.
- [48] R. W. GASKELL et al., "Characterizing and navigating small bodies with imaging data," *Meteoritics & Planetary Science*, vol. 43, no. 6. Wiley, pp. 1049-1061, Jun. 2008. doi: 10.1111/j.1945-5100.2008.tb00692.x.
- [49] V. Lohse, C. Heipke, and R. L. Kirk, "Derivation of planetary topography using multi-image shape-from-shading," *Planetary and Space Science*, vol. 54, no. 7. Elsevier BV, pp. 661-674, Jul. 2006. doi: 10.1016/j.pss.2006.03.002.
- [50] O. Alexandrov and R. A. Beyer, "Multiview Shape-From-Shading for Planetary Images," *Earth and Space Science*, vol. 5, no. 10. American Geophysical Union (AGU), pp. 652-666, Oct. 2018. doi: 10.1029/2018ea000390.
- [51] B. Wu, W. C. Liu, A. Grumpe, and C. Wöhler, "Construction of pixel-level resolution DEMs from monocular images by shape and albedo from shading constrained with low-resolution DEM," *ISPRS Journal of Photogrammetry and Remote Sensing*, vol. 140. Elsevier BV, pp. 3-19, Jun. 2018. doi: 10.1016/j.isprsjprs.2017.03.007.
- [52] C. Jiang, S. Douté, B. Luo, and L. Zhang, "Fusion of photogrammetric and photoclinoetry information for high-resolution DEMs from Mars in-orbit imagery," *ISPRS Journal of Photogrammetry and Remote Sensing*, vol. 130. Elsevier BV, pp. 418-430, Aug. 2017. doi: 10.1016/j.isprsjprs.2017.06.010.
- [53] R. L. Kirk, D. P. Mayer, C. M. Dundas, B. H. Wheeler, R. A. Beyer, and O. Alexandrov, "COMPARISON OF DIGITAL TERRAIN MODELS FROM TWO PHOTOCALINOMETRY METHODS," *The International Archives of the Photogrammetry, Remote Sensing and Spatial Information Sciences*, vol. XLIII-B3-2022. Copernicus GmbH, pp. 1059-1067, May 30, 2022. doi: 10.5194/isprs-archives-xxliii-b3-2022-1059-2022.
- [54] K. Di, J. Oberst, I. Karachetseva, and B. Wu, "TOPOGRAPHIC MAPPING OF THE MOON IN THE 21ST CENTURY: FROM HECTOMETER TO MILLIMETER SCALES," *The International Archives of the Photogrammetry, Remote Sensing and Spatial Information Sciences*, vol. XLIII-B3-2020. Copernicus GmbH, pp. 1117-1124, Aug. 21, 2020. doi: 10.5194/isprs-archives-xxliii-b3-2020-1117-2020.
- [55] H. Chen et al., "CNN-Based Large Area Pixel-Resolution Topography Retrieval From Single-View LROC NAC Images Constrained With SL-DEM," *IEEE Journal of Selected Topics in Applied Earth Observations and Remote Sensing*, vol. 15. Institute of Electrical and Electronics Engineers (IEEE), pp. 9398-9416, 2022. doi: 10.1109/jstars.2022.3214926.
- [56] H. Chen, X. Hu, and J. Oberst, "PIXEL-RESOLUTION DTM GENERATION FOR THE LUNAR SURFACE BASED ON A COMBINED DEEP LEARNING AND SHAPE-FROM-SHADING (SFS) APPROACH," *ISPRS Annals of the Photogrammetry, Remote Sensing and Spatial Information Sciences*, vol. V-3-2022. Copernicus GmbH, pp. 511-516, May 17, 2022. doi: 10.5194/isprs-annals-v-3-2022-511-2022.
- [57] H. Chen et al., "ELunarDTMNet: Efficient Reconstruction of High-Resolution Lunar DTM From Single-View Orbiter Images," *IEEE Transactions on Geoscience and Remote Sensing*, vol. 62. Institute of Electrical and Electronics Engineers (IEEE), pp. 1-20, 2024. doi: 10.1109/tgrs.2024.3501153.
- [58] Liu, Z., Lin, Y., Cao, Y., Hu, H., Wei, Y., Zhang, Z., Lin, S. and Guo, B., 2021. "Swin transformer: Hierarchical vision transformer using shifted windows," in *Proceedings of the IEEE/CVF international conference on computer vision* (pp. 10012-10022).
- [59] Z. Chen, B. Wu, and W. C. Liu, "Mars3DNet: CNN-Based High-Resolution 3D Reconstruction of the Martian Surface from Single Im-

- ages.” *Remote Sensing*, vol. 13, no. 5. MDPI AG, p. 839, Feb. 24, 2021. doi: 10.3390/rs13050839.
- [60] Y. Tao et al., “Rapid Single Image-Based DTM Estimation from ExoMars TGO CaSSIS Images Using Generative Adversarial U-Nets,” *Remote Sensing*, vol. 13, no. 15. MDPI AG, p. 2877, Jul. 22, 2021. doi: 10.3390/rs13152877.
- [61] Y. Tao, J.-P. Muller, S. Xiong, and S. J. Conway, “MADNet 2.0: Pixel-Scale Topography Retrieval from Single-View Orbital Imagery of Mars Using Deep Learning,” *Remote Sensing*, vol. 13, no. 21. MDPI AG, p. 4220, Oct. 21, 2021. doi: 10.3390/rs13214220.
- [62] Y. Tao, J.-P. Muller, S. J. Conway, S. Xiong, S. H. G. Walter, and B. Liu, “Large Area High-Resolution 3D Mapping of the Von Kármán Crater: Landing Site for the Chang’E-4 Lander and Yutu-2 Rover,” *Remote Sensing*, vol. 15, no. 10. MDPI AG, p. 2643, May 18, 2023. doi: 10.3390/rs15102643.
- [63] Y. Tao, S. H. G. Walter, J. Muller, Y. Luo, and S. Xiong, “A High-Resolution Digital Terrain Model Mosaic of the Mars 2020 Perseverance Rover Landing Site at Jezero Crater,” *Earth and Space Science*, vol. 10, no. 10. American Geophysical Union (AGU), Oct. 2023. doi: 10.1029/2023ea003045.
- [64] J. Cao, R. Huang, Z. Ye, Y. Xu, and X. Tong, “Generative 3D Reconstruction of Martian Surfaces using Monocular Images,” *The International Archives of the Photogrammetry, Remote Sensing and Spatial Information Sciences*, vol. XLVIII-3-2024. Copernicus GmbH, pp. 51-56, Nov. 07, 2024. doi: 10.5194/isprs-archives-xxviii-3-2024-51-2024.
- [65] L. Yang, Z. Zhu, L. Sun, and D. Zhang, “Global Attention-Based DEM: A Planet Surface Digital Elevation Model-Generation Method Combined with a Global Attention Mechanism,” *Aerospace*, vol. 11, no. 7. MDPI AG, p. 529, Jun. 28, 2024. doi: 10.3390/aerospace11070529.
- [66] Y. LeCun, Y. Bengio, and G. Hinton, “Deep learning,” *Nature*, vol. 521, no. 7553. Springer Science and Business Media LLC, pp. 436-444, May 27, 2015. doi: 10.1038/nature14539.
- [67] G. E. Hinton and R. R. Salakhutdinov, “Reducing the Dimensionality of Data with Neural Networks,” *Science*, vol. 313, no. 5786. American Association for the Advancement of Science (AAAS), pp. 504-507, Jul. 28, 2006. doi: 10.1126/science.1127647.
- [68] D. P. Kingma and M. Welling, “Auto-Encoding Variational Bayes,” 2013, arXiv. doi: 10.48550/ARXIV.1312.6114.
- [69] W. Hu, Y. Huang, L. Wei, F. Zhang, and H. Li, “Deep Convolutional Neural Networks for Hyperspectral Image Classification,” *Journal of Sensors*, vol. 2015. Wiley, pp. 1-12, 2015. doi: 10.1155/2015/258619.
- [70] B. Moseley, V. Bickel, J. Burelbach, and N. Relatores, “Unsupervised Learning for Thermophysical Analysis on the Lunar Surface,” *The Planetary Science Journal*, vol. 1, no. 2. American Astronomical Society, p. 32, Jul. 28, 2020. doi: 10.3847/psj/ab9a52.
- [71] Lesnikowski, Adam, Valentin T. Bickel, and Daniel Angerhausen, “Automated Discovery of Anomalous Features in Ultra-Large Planetary Remote Sensing Datasets using Variational Autoencoders,” *IEEE Journal of Selected Topics in Applied Earth Observations and Remote Sensing*, 2024.
- [72] C. Yang et al., “Lunar impact crater identification and age estimation with Chang’E data by deep and transfer learning,” *Nature Communications*, vol. 11, no. 1. Springer Science and Business Media LLC, Dec. 22, 2020. doi: 10.1038/s41467-020-20215-y.
- [73] Y. Qian et al., “Copernican-Aged (< 200 Ma) Impact Ejecta at the Chang’e-5 Landing Site: Statistical Evidence From Crater Morphology, Morphometry, and Degradation Models,” *Geophysical Research Letters*, vol. 48, no. 20. American Geophysical Union (AGU), Oct. 19, 2021. doi: 10.1029/2021gl095341.
- [74] Vaswani, A. “Attention is all you need.” *Advances in Neural Information Processing Systems* (2017).
- [75] Van Den Oord, Aaron, and Oriol Vinyals. “Neural discrete representation learning,” 2017, *Advances in neural information processing systems* 30.
- [76] G. Sharir, A. Noy, and L. Zelnik-Manor, “An Image is Worth 16x16 Words, What is a Video Worth?,” 2021, arXiv. doi: 10.48550/ARXIV.2103.13915.
- [77] W. Peebles, and X. Saining., “Scalable diffusion models with transformers,” In *Proceedings of the IEEE/CVF International Conference on Computer Vision*, pp. 4195-4205, 2023.
- [78] S. Atito, M. Awais, and J. Kittler, “SiT: Self-supervised vision Transformer,” 2021, arXiv. doi: 10.48550/ARXIV.2104.03602.
- [79] D. Pathak, P. Krahenbuhl, J. Donahue, T. Darrell, and A. A. Efros, “Context Encoders: Feature Learning by Inpainting,” arXiv, 2016, doi: 10.48550/ARXIV.1604.07379.
- [80] K. He, X. Chen, S. Xie, Y. Li, P. Dollár, and R. Girshick, “Masked Autoencoders Are Scalable Vision Learners,” 2022 *IEEE/CVF Conference on Computer Vision and Pattern Recognition (CVPR)*. IEEE, Jun. 2022. doi: 10.1109/cvpr52688.2022.01553.
- [81] Lu, Jiasen, Christopher Clark, Rowan Zellers, Roozbeh Mottaghi, and Aniruddha Kembhavi. “Unified-io: A unified model for vision, language, and multi-modal tasks.” In *The Eleventh International Conference on Learning Representations*. 2022.
- [82] J. Lu et al., “Unified-IO 2: Scaling Autoregressive Multimodal Models with Vision, Language, Audio, and Action,” 2024 *IEEE/CVF Conference on Computer Vision and Pattern Recognition (CVPR)*. IEEE, pp. 26429-26445, Jun. 16, 2024. doi: 10.1109/cvpr52733.2024.02497.
- [83] R. Bachmann, D. Mizrahi, A. Atanov, and A. Zamir, “MultiMAE: Multi-modal Multi-task Masked Autoencoders,” *Lecture Notes in Computer Science*. Springer Nature Switzerland, pp. 348-367, 2022. doi: 10.1007/978-3-031-19836-6\_20.
- [84] Mizrahi, David, Roman Bachmann, Oguzhan Kar, Teresa Yeo, Mingfei Gao, Afshin Dehghan, and Amir Zamir. “4m: Massively multimodal masked modeling,” 2024, *Advances in Neural Information Processing Systems* 36.
- [85] R. Bachmann et al., “4M-21: An Any-to-Any Vision Model for Tens of Tasks and Modalities,” 2024, arXiv. doi: 10.48550/ARXIV.2406.09406.
- [86] Panambur, T., Sander, T., Wohlfarth, K., Martinot, M., Zorzan, S., Parente, M., Bishop, J.L. and Wöhler, C., “Using machine learning to find relationships between different lunar maps: A case study of lunar hydration,” 2024, *AGU Fall Meeting Abstracts*. <https://ui.adsabs.harvard.edu/abs/2024AGUFMIN51B..06P>
- [87] Sander, T., Wöhler, C., “Lunar Image Transformation: A Multi-Modal Any-To-Any Generation Approach,” March 2025, 56th Lunar and Planetary Science Conference 2025 (LPSC). <https://www.hou.usra.edu/meetings/lpsc2025/pdf/1159.pdf>
- [88] Nedungadi, V., Kariyaa, A., Oehmcke, S., Belongie, S., Igel, C. and Lang, N., 2024, September, “MMEarth: Exploring multi-modal pretext tasks for geospatial representation learning,” In *European Conference on Computer Vision* (pp. 164-182). Cham: Springer Nature Switzerland.
- [89] Blumenstiel, B., Fraccaro, P., Marsocci, V., Jakubik, J., Maurogiovanni, S., Czerkawski, M., Sedona, R., Cavallaro, G., Brunswiler, T., Bernabe-Moreno, J. and Longépé, N., 2025. “TerraMesh: A Planetary Mosaic of Multimodal Earth Observation Data,” arXiv preprint arXiv:2504.11172.
- [90] J. Jakubik et al., “TerraMind: Large-Scale Generative Multimodality for Earth Observation,” 2025, arXiv. doi: 10.48550/ARXIV.2504.11171.
- [91] M. S. Robinson et al., “Lunar Reconnaissance Orbiter Camera (LROC) Instrument Overview,” *Space Science Reviews*, vol. 150, no. 1-4. Springer Science and Business Media LLC, pp. 81-124, Jan. 2010. doi: 10.1007/s11214-010-9634-2.
- [92] D. C. Humm et al., “Flight Calibration of the LROC Narrow Angle Camera,” *Space Science Reviews*, vol. 200, no. 1-4. Springer Science and Business Media LLC, pp. 431-473, Sep. 21, 2015. doi: 10.1007/s11214-015-0201-8.
- [93] T. Sucharski et al., *USGS-Astrogeology/ISIS3: ISIS 4.2.0 Public Release*. Zenodo, 2020. doi: 10.5281/ZENODO.3962369.
- [94] S. J. Koppal, “Lambertian Reflectance,” *Computer Vision*. Springer US, pp. 441-443, 2014. doi: 10.1007/978-0-387-31439-6\_534.
- [95] Loshchilov, I. and Hutter, F., “Decoupled Weight Decay Regularization,” 2017, In *International Conference on Learning Representations*.
- [96] Loshchilov, I. and Hutter, F., “SGDR: Stochastic Gradient Descent with Warm Restarts,” 2022, July, In *International Conference on Learning Representations*.

## APPENDIX

This appendix provides additional details on the data handling, tokenizer architecture, and model architecture used in this study. The sections are organized as follows:

- **Appendix A:** Data handling and preparation
- **Appendix B:** Tokenizer architecture and training details
- **Appendix C:** Model architecture and training details
- **Appendix D:** Shape from Shading regularization terms

Parameter:	Modality			
	Gray	DEM	Normals	Albedo
vocab_size	1536	2048	1536	1024
decay			0.99	
use_ema			True	
imgSize			224 × 224	
patch_size			8 × 8	
embedding_dim			128	
enc_num_heads			4	
enc_num_layers			6	
dec_conv_dim			64	
#parameters	1.5M	1.6M	1.5M	1.5M

TABLE III: Parameters of tokenizer architecture for all modalities. The parameters are the same for all modalities, except for the vocab\_size.

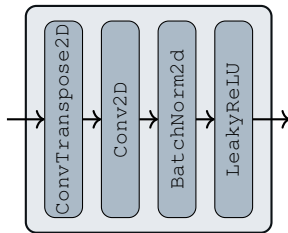


Fig. 9: This figure shows a single decoder building block consisting of a ConvTranspose2D layer, followed by a Conv2D layer, BatchNormalization2D, and a LeakyReLU activation function.

## APPENDIX A

### DATA HANDLING AND PREPERATION

Normalization is a crucial step in preparing the data for training and evaluation. The following normalization techniques were applied to different data types:

- **Gray:** `torchvision → Normalize(...)`
- **DEM:** Subtracting mean from each image
- **Normals:** None
- **Albedo:** `torchvision → Normalize(...)`

All data types were stroed in pixelwise ontop of each other.

## APPENDIX B

### TOKENIZER ARCHITECTURE AND TRAINING DETAILS

All tokenizer architectures share a common structure that incorporates a Vision Transformer (ViT) encoder, which is configured identically across all modalities. This includes parameters such as embedding dimension, number of attention heads, and number of transformer layers (see Table III). A consistent upsampling convolutional neural network (UpConv CNN) serves as the decoder for each modality (see Figure 9 for each UConv Block structure). Additionally, the central Vector Quantization (VQ) layer maintains the same decay rate and uses an exponential moving average (EMA).

The main difference between the tokenizers is the size of their vocabularies, which are customized to suit the unique characteristics and complexity of each input modality: grayscale images, Digital Elevation Models (DEMs), surface normals, and albedo maps. This tailored approach to vocabulary size enables each tokenizer to effectively learn a discrete

Parameter:	Value:
batch_size	128
num_epochs	64

TABLE IV: Training parameters of the tokenizer.

latent space that is both efficient and representative of its specific data type while still utilizing the shared encoder-decoder backbone for consistent feature extraction and reconstruction.

Furthermore, all tokenizers are trained with a batch size of 128 and 64 epochs, as shown in Table IV.

## APPENDIX C

### MODEL ARCHITECTURE AND TRAINING DETAILS

Table V presents a detailed overview of the key hyperparameters used in training the multimodal model that follows the 4M Architecture. The optimization process utilized the AdamW optimizer [95] with  $\beta$  parameters set to (0.9, 0.99). The initial learning rate was set to  $5 \cdot 10^{-5}$ , and a weight decay of 0.05 was applied. To ensure training stability, gradient clipping was implemented with a maximum norm of 3.0. The learning rate schedule adhered to a Cosine Annealing strategy [96], featuring a maximum cycle length (Tmax) of 5 epochs and a minimum learning rate of  $5 \cdot 10^{-8}$ .

The model’s embedding dimension was established at 384, with embedding weights initialized using a normal distribution that has a standard deviation of 0.15. The loss function used was of the ‘mod’ type (the specific formulation of this loss is elaborated in Section IV-C). Both the number of input and target tokens was set to 2358.

Within the Transformer architecture of the 4M model, 6 attention heads were utilized in the multi-head attention layers. The encoder and decoder components each consisted of 6 layers, with bias terms explicitly disabled in the projection (`proj_bias`) and query-key-value (`qkv_bias`) layers. Additionally, a gated multi-layer perceptron (`gated_mlp`) was incorporated within the feed-forward network of the Transformer blocks. The model made use of pre-trained weights according to the 4M architecture<sup>1</sup> (`pretrained4M = True`).

In total, the resulting model contains 29.7 million trainable parameters, with 10.6 million in the encoder, 14.2 million in the decoder, and 2.4 million in each of the encoder and decoder embedding layers.

## APPENDIX D

### SHAPE FROM SHADING REGULARIZATION TERMS

Because the choice of regularization terms affects the results of the SfS algorithm, we provide a brief description of the regularization terms used in this work. We adopt the integrability error

$$E_{\text{int}} = \frac{1}{2} \int_x \int_y \left( \frac{\partial z}{\partial x} - p \right)^2 + \left( \frac{\partial z}{\partial y} - q \right)^2 dx dy \quad (12)$$

introduced by Horn [41] to enforce integrability of the noisy gradient field.

<sup>1</sup>We modified the code of the 4M Model for our experiments. The code of the original model can be found on GitHub: <https://github.com/apple/ml-4m/>

Parameter:	Value:
optimizer	AdamW
betas	(0.9, 0.99)
learning_rate	$5 \cdot 10^{-5}$
weight_decay	0.05
gradient_clip_value	3.0
scheduler	CosineAnnealingLR(...)
↳ T_max	5
↳ eta_min	$5 \cdot 10^{-8}$
embed_dim	384
embedding_init_std	0.15
loss_type	mod
num_input_tokens	2352
num_target_tokens	2352
num_heads	6
encoder_depth	6
decoder_depth	6
proj_bias	False
qkv_bias	False
gated_mlp	True
pretrained4M	True
#encoder_parameters	10.6M
#decoder_parameters	14.2M
#encoder_embed_parameters	2.4M
#decoder_embed_parameters	2.4M
#total_parameters	29.7M

TABLE V: Hyperparameters of the multimodal model.

Shape from shading can accurately estimate the surface slope, but the absolute height is not well constrained without a suitable initialization. We restrict the deviation of the estimated DEM from the initial DEM  $z_{\text{DEM}}$  [28] with two additional regularization terms introduced by [44]. The relative depth constraint is given by

$$E_{\text{rel}} = \frac{1}{2} \int_x \int_y \left( f(p) - f\left(\frac{\partial z_{\text{DEM}}}{\partial x}\right) \right)^2 + \left( f(q) - f\left(\frac{\partial z_{\text{DEM}}}{\partial y}\right) \right)^2 dx dy \quad (13)$$

with a low-pass filter  $f$  to match the image resolution to the lower DEM resolution.

The absolute depth constraint

$$E_{\text{abs}} = \frac{1}{2} \int_x \int_y (f(z) - f(z_{\text{DEM}}))^2 dx dy \quad (14)$$

ensures that the low-frequency components of the DEM are similar to the initial DEM. The total error to be minimized is the weighted sum of the individual error terms:

$$E_{\text{total}} = E_{\text{I}} + \gamma E_{\text{int}} + \delta E_{\text{rel}} + \tau E_{\text{abs}} \quad (15)$$